Photon-Induced Weyl Half-Metal Phase and Spin Filter Effect from Topological Dirac Semimetals

Xiao-Shi Li,[1] Chen Wang,[3] Ming-Xun Deng,[1,*] Hou-Jian Duan,[1] Pei-Hao Fu,[1] Rui-Qiang Wang,[1,†] L. Sheng,[2] and D. Y. Xing[2,‡]

[1]*Guangdong Provincial Key Laboratory of Quantum Engineering and Quantum Materials, GPETR Center for Quantum Precision Measurement, SPTE, South China Normal University, Guangzhou 510006, China*

[2]*National Laboratory of Solid State Microstructures and Department of Physics, Nanjing University, Nanjing 210093, China*

[3]*Lab for Computational Imaging Technology and Engineering, School of Electronic Science and Engineering, Nanjing University, Nanjing 210023, China*

(Received 1 May 2019; revised manuscript received 6 September 2019; published 15 November 2019)

Recently discovered Dirac semimetals (DSMs) with two Dirac nodes, such as Na_3Bi and Cd_2As_3, are regarded as carrying the $\mathbb{Z}_2$ topological charge in addition to the chiral charge. We study the Floquet phase transition of $\mathbb{Z}_2$ topological DSMs subjected to a beam of circularly polarized light. Owing to the resulting interplay of the chiral and $\mathbb{Z}_2$ charges, the Weyl nodes are not only chirality dependent but also spin dependent, which constrains the behavior in creation and annihilation of the pair of Weyl nodes. Interestingly, we find a novel phase: One spin band is in the Weyl semimetal phase while the other is in the insulator phase, and we dub it the Weyl half-metal (WHM) phase. We further study the spin-dependent transport in a Dirac-Weyl semimetal junction and find a spin filter effect as a fingerprint of the existence of the WHM phase. The proposed spin filter effect, based on the WHM bulk band, is highly tunable in a broad parameter regime and robust against magnetic disorder, which is expected to overcome the shortcomings of the previously proposed spin filter based on the topological edge or surface states. Our results offer a unique opportunity to explore the potential applications of topological DSMs in spintronics.

DOI: 10.1103/PhysRevLett.123.206601

Great interest recently has been triggered in spintronics toward three-dimensional (3D) topological semimetal materials [1,2], such as Dirac semimetals (DSMs) and Weyl semimetals (WSMs). A DSM is a 3D counterpart of graphene, in which the conduction and valence bands touch, near the Fermi surface, at a certain discrete Dirac point (DP). The DPs are usually unstable because of the strong repulsion between degenerate bands [3,4]. By breaking the time-reversal (TR) or spatial-inversion symmetry, a single DP can split into a pair of Weyl nodes, leading to the phase transition from a DSM to a WSM [5–7].

According to the classification [3], there are two distinct classes of 3D DSMs: One class is the topologically trivial DSMs possessing a single DP at a time-reversal invariant momentum, and the other is the topologically nontrivial DSMs possessing a pair of DPs created by band inversion, such as Na_3Bi [2] and Cd_2As_3 [8] compounds. Usually, the dispersion of the nodes is described by the momentum coupled to pseudospin, while the real spin is suppressed due to spin degeneracy. Nevertheless, in topological DSMs Na_3Bi and Cd_2As_3, there is well-defined real spin, and two Weyl nodes at each DP are spin resolved. Since the Weyl nodes belong to different irreducible representations, two Weyl nodes at the same DP cannot be coupled as a pair and have to seek a partner with the same spin from the other DP. As a consequence, the two DPs including two pairs of Weyl nodes, separated by a net momentum in the Brillouin zone (BZ), are connected by two spin-polarized Fermi arcs [2,3,9–11]. This scenario resembles the topological insulators, carrying a nontrivial $\mathbb{Z}_2$ topological charge, and thus was named $\mathbb{Z}_2$ topological DSMs [4,12].

To explore the unique properties of DSMs and WSMs from transport measurements, many works [13–18] have been devoted to the longitudinal negative magnetoresistance effect due to the chiral anomaly. In addition to the chiral anomaly, the $\mathbb{Z}_2$ DSMs also carry a $\mathbb{Z}_2$ topological charge, exhibiting the $\mathbb{Z}_2$ quantum anomaly [12]. A natural question to ask in this regard is whether the existence of the $\mathbb{Z}_2$ topological charge also manifests itself in any way in transport. Burkov and Kim [12] addressed the finding that in magnetotransport, the $\mathbb{Z}_2$ topological order manifested as the narrowing dependence of the positive magnetoconductivity, which provides a possible explanation for a recent experiment [13]. Besides, the influence of interplay between the $\mathbb{Z}_2$ and chiral anomalies on magnetoconductivity has been studied in a relativistic hydrodynamics limit [19].

The main objective of our work is to exploit the joint influence of $\mathbb{Z}_2$ topological and chiral charges on spin transport. In this Letter, we apply a beam of circularly polarized light (CPL), which is widely adopted to induce

topological phase transitions of matter [20–26], to drive the phase transition of $\mathbb{Z}_2$ DSMs. We find that CPL can first create and then annihilate a pair of Weyl nodes and finally gap them out, during which time the node pairs associated with different spin orientations exhibit different responses to CPL. Consequently, the $\mathbb{Z}_2$ DSM can be driven into a Weyl half-metal (WHM) phase. Based on this, we further analyze the spin-dependent transport in a Dirac-Weyl semimetal junction and find that the existence of the WHM phase is manifested as a fully spin-polarized current, i.e., the spin filter effect. The half-metallicity was recently employed to realize fully spin polarized Weyl loops or magnetic topological semimetal states [27,28].

Floquet effective Hamiltonian.—Let us start with a four-band effective Hamiltonian

$$H(\mathbf{k}) = \epsilon_0(\mathbf{k}) + M(\mathbf{k})\tau_z + v_0(k_x\sigma_z\tau_x - k_y\tau_y) + \frac{B_3 k_z}{2}(k_+^2\sigma_- + k_-^2\sigma_+)\tau_x, \quad (1)$$

with $k_\pm = k_x \pm ik_y$ and $\sigma_\pm = \sigma_x \pm i\sigma_y$, which is widely adopted to describe topological properties of $\mathbb{Z}_2$ topological DSMs Na_3Bi [9] and Cd_3As_2 [10]. Here, $\sigma_{x,y,z}$ ($\tau_{x,y,z}$) are Pauli matrices for the electron spin (orbital parity or pseudospin), $\epsilon_0(\mathbf{k}) = C_0 + C_1k_z^2 + C_2(k_x^2 + k_y^2)$, and $M(\mathbf{k}) = M_0 - M_1k_z^2 - M_2(k_x^2 + k_y^2)$, with C_j, M_j, B_3, and v_0 as material parameters. If we concentrate only on the neighborhood of each gap-crossing point and neglect the high-order terms B_3, Hamiltonian (1) describes two superimposed copies of WSMs, related, respectively, to two spin species, which is a conserved quantity. It is easy to find that, for $M_0/M_1 > 0$, there exist two DPs at $\mathbf{k}_c = (0, 0, \pm\sqrt{M_0/M_1})$, each of which contains two spin-resolved Weyl nodes. It is distinct from an ordinary DSM that the two Weyl nodes at the same DP here are nonpaired since two Weyl sectors are protected from mixing by the $\mathbb{Z}_2$ symmetry. The $\mathbb{Z}_2$ DSM structure is confirmed by the existence of two surface Fermi arcs, as shown in Fig. 1(a), connecting the two paired Weyl nodes from different DPs. The spin texture of the surface states has a helical structure, resembling the surface states of topological insulators.

When a beam of CPL irradiates along the direction $\mathbf{n} = (\sin\theta\cos\phi, \sin\theta\sin\phi, \cos\theta)$ as illustrated in Fig. 1(b), where θ and ϕ are the polar and azimuthal angles in the spherical coordinate system, the Dirac fermions can be described by a time-dependent Hamiltonian $\mathcal{H}(\mathbf{k}, t) = H(\mathbf{k} + e\mathbf{A}/\hbar)$, where

$$\mathbf{A} = A_0[\cos(\omega t)\mathbf{e}_1 - \eta\sin(\omega t)\mathbf{e}_2] \quad (2)$$

is vector potential for CPL with amplitude A_0, frequency ω, and $\eta = \pm 1$ for right or left polarization. Here, the spatial dependence of $\mathbf{A}$ is not important, and a careful discussion on the spatial dependence is presented in the Supplemental Material [29]. Here, $\mathbf{e}_1 = (\cos\theta\cos\phi, \cos\theta\sin\phi, -\sin\theta)$ and $\mathbf{e}_2 = (\sin\phi, -\cos\phi, 0)$, satisfying $\mathbf{e}_1 \cdot \mathbf{e}_2 = 0$, are two unit vectors perpendicular to the incident direction of the light. Employing the Floquet theorem [20–26,30] and focusing on the off-resonant regime, in which $\hbar\omega$ is greater than the width of the static energy band, we derive an effective Hamiltanion [29],

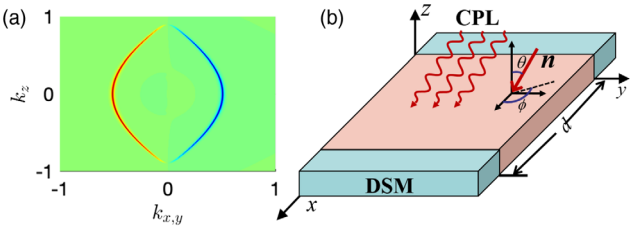

FIG. 1. (a) Spin-resolved Dirac points connected by two Fermi arcs projected on a $k_z - k_{x,y}$ plane in a $\mathbb{Z}_2$ topological DSM. The filled colors denote the magnitude of the averaged surface spin density of states $\langle\sigma_z\rangle$, with red, green, and blue for $\langle\sigma_z\rangle\{>, =, <\}0$, respectively. (b) Schematic illustration of the DSM-WSM tunnel junction in which the middle region ($0 < x < d$) is irradiated by a beam of CPL along direction $\mathbf{n} = (\sin\theta\cos\phi, \sin\theta\sin\phi, \cos\theta)$, where θ and ϕ are the polar and azimuthal angles in the spherical coordinate system.

$$\mathcal{H}_{\text{eff}}(\mathbf{k}) = \tilde{\epsilon}_0(\mathbf{k}) + \tilde{M}(\mathbf{k})\tau_z + v_0(k_x\sigma_z\tau_x - k_y\tau_y) - \lambda\sigma_z\tau_z + v_1k_z(\cos\phi\tau_x - \sin\phi\sigma_z\tau_y) - v_2(k_x\tau_x - k_y\sigma_z\tau_y), \quad (3)$$

where B_3 is dropped due to smallness, and denote $\lambda = \eta(v_0^2k_A^2\cos\theta/\omega)$, $v_1 = \eta(2M_1k_A^2\sin\theta/\omega)v_0$, and $v_2 = \eta(2M_2k_A^2\cos\theta/\omega)v_0$, with $k_A = eA_0/\hbar$ characterizing the CPL intensity. The renormalized parameters in the first two terms are given by $\tilde{\epsilon}_0(\mathbf{k}) = \epsilon_0(\mathbf{k})|_{C_0 \to C_0 + C_0'}$ and $\tilde{M}(\mathbf{k}) = M(\mathbf{k})|_{M_0 \to M_0 - M_0'}$, where $C_0' = k_A^2\{[(1+\eta^2)/2]C_2 + C_-\sin^2\theta\}$ and $M_0' = k_A^2\{[(1+\eta^2)/2]M_2 + M_-\sin^2\theta\}$, with $C_- = (C_1 - C_2)/2$ and $M_- = (M_1 - M_2)/2$.

CPL-driven WHM phase.—As shown, in the presence of CPL, the TR symmetry is broken explicitly such that the DPs are expected to split into two pairs of spin-resolved Weyl nodes. The quasienergy spectrum of the effective Hamiltonian (3) is

$$\epsilon_{s,\pm}(\mathbf{k}) = \tilde{\epsilon}_0(\mathbf{k}) \pm \sqrt{|\tilde{M}_s(\mathbf{k})|^2 + v_s^2(\tilde{k}_{x,s}^2 + \tilde{k}_{y,s}^2)}, \quad (4)$$

where $\tilde{k}_{x,s} = k_x + s(v_1/v_s)k_z\cos\phi$ and $\tilde{k}_{y,s} = k_y + s(v_1/v_s)k_z\sin\phi$, with $v_s = v_0 - sv_2$ and $\tilde{M}_s(\mathbf{k}) = \tilde{M}(\mathbf{k}) - s\lambda$. In contrast to the static spectrum of Hamiltonian (1), the CPL-driven spectrum becomes spin dependent. The evolution of the spin-resolved quasienergy spectrum with CPL intensity is plotted in Fig. 2(a). There are four Weyl nodes located at

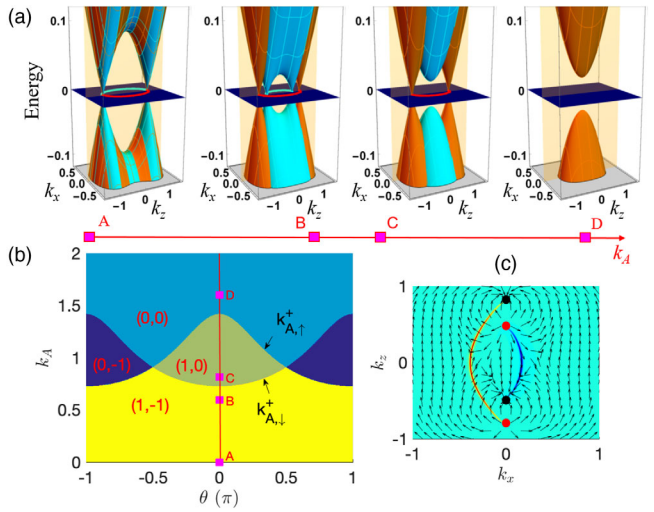

FIG. 2. (a) Evolution of the spin-resolved quasienergy spectrum with the CPL intensity $k_A = (0, 0.6, 0.8, 1.6) \times \mathrm{nm}^{-1}$ from the left to the right side, which correspond to points A–D marked in (b). The other CPL parameters are $\hbar\omega = 1.0$ eV [31,32], $\phi = 0$, and $\theta = 0$. The brown and blue regions represent the spin-↑ and spin-↓ Weyl sectors, respectively, and the lines connecting the nodes denote the surface Fermi arcs. (b) The phase diagram characterized with the spin-dependent Chern fluxes $(C_\uparrow, C_\downarrow)$ in the $k_A - \theta$ parameter space, and (c) the Berry curvature distribution corresponding to point B, where the red and black circles stand for the Weyl nodes with positive and negative chiral charges, respectively. The calculation is carried out for Na_3Bi, whose parameters can be found in Ref. [9].

$$\mathbf{k}^s_{c,\pm} = \pm(sv_1\cos\phi, sv_1\sin\phi, -v_s)k_{w,s}/v_s, \tag{5}$$

with $k_{w,s} = \sqrt{[M_0 - (M_0' + s\lambda)]/[M_1 + v_1^2 M_2/v_s^2]}$, which correspond to the vertexes of the dispersion. In the presence of CPL, the two Weyl nodes overlapping at one DP are separated and, simultaneously, the Berry curvature emerges in the whole momentum space, starting from a Weyl node with positive chiral charge and ending at one with negative chiral charge [see Fig. 2(c)]. Notice that the split Weyl nodes are not only chirality dependent but also spin dependent, as shown in Fig. 2(a), where the brown and blue regions represent spin ↑ and spin ↓, respectively, and two nodes with the same spin are connected by an open Fermi arc. Importantly, with an increase of k_A, the distance $2k_{w,s}$ between the paired Weyl nodes would reduce because of the CPL-renormalized term M_0'. Consequently, at a certain crucial value, the paired Weyl nodes with opposite chirality can be merged in momentum space and then gapped out. Notice that the different spin species have different critical values, which originate from the renormalized spin-dependent Dirac mass term $s\lambda$. It is interesting to find a phase as illustrated in the third diagram of Fig. 2(a), where the spin-↑ species still remains at the WSM phase but the spin-↓ species enters the insulator phase, which exhibits a typical characteristic of well-known spin half-metals. This novel Weyl phase has not been reported before, and we dub it the WHM phase. As k_A further increases, both pairs of the Wely nodes could be gapped out, and finally the system undergoes a transition to an insulating phase, as shown in the last diagram of Fig. 2(a).

In order to identify these different topological phases, we can further classify them according to the spin-dependent Chern fluxes $(C_\uparrow, C_\downarrow)$ at the $k_z = 0$ BZ cross section [3]. With the Berry curvature [4] $\Omega_{s,ij}(\mathbf{k}) = (1/2|d_s|^3)\epsilon_{abc}d_{s,a}\partial_i d_{s,b}\partial_j d_{s,c}$, where ϵ_{abc} denotes the antisymmetric tensor and $d_s = [sv_0\tilde{k}_{x,s}, v_0\tilde{k}_{y,s}, \tilde{M}_s(\mathbf{k})]$, we find

$$C_s = -\frac{s}{2}[\mathrm{sgn}(M_2) + \mathrm{sgn}(M_0 - M_0' - s\lambda)] \tag{6}$$

for the s spin component. In Fig. 2(b), we plot the phase diagram in the $k_A - \theta$ parameter space. From the bottom to the top, e.g., points A to D, the phases are, in order, the DSM phase ($k_A = 0$), the WSM phase $(1, -1)$, the WHM phase (1,0) or $(0, -1)$, and the normal insulating phase (0,0), whose dispersions are depicted in Fig. 2(a). The phase boundaries are determined by the equation $M_2 + M_- \sin^2\theta + s\eta v_0^2\cos\theta/\omega = M_0/k_A^2$ via $k_{w,s} = 0$. Subsequently, we can derive the crucial values for the light intensity to be

$$k^\eta_{A,s} = \sqrt{\frac{M_0}{M_2 + M_-\sin^2\theta + s\eta v_0^2\cos\theta/\omega}}. \tag{7}$$

The WHM phase emerges in the range of $(k^+_{A,\downarrow}, k^+_{A,\uparrow})$ for $|\theta| < \pi/2$, where only the spin-↑ WHM phase exists. The spin-↓ WHM phase can be realized just by reversing the polarization η of the CPL or by tuning the incident direction $|\theta| > \pi/2$ to be in the WHM region $(0, -1)$. If $k_A > k^+_{A,\uparrow}$, the CPL-driven DSM would cross over to a normal insulator with spin-dependent Chern fluxes (0,0), where both pairs of the Weyl nodes are gapped out. Also, we can tune the thresholds $k^+_{A,\downarrow}$ and $k^+_{A,\uparrow}$ by changing the incident direction of the CPL due to the rotation of the Weyl nodes in the $k_x - k_z$ plane. For a specific value $\theta = \pm\pi/2$, the thresholds $k^+_{A,\downarrow} = k^+_{A,\uparrow}$, and thus the WHM phase region vanishes.

CPL-modulated spin-dependent transmission.—In the following, we study the transport fingerprint related to the WHM phase. We construct a DSM-WSM sandwich junction, as shown in Fig. 1(b), where the middle WSM region $0 < x < d$ is formed due to the irradiation by a beam of CPL. The eigenequation for the DSM reservoirs can be obtained as

$$[E - \epsilon_0(\mathbf{k})]^2 = [M(\mathbf{k})]^2 + v_0^2(k_x^2 + k_y^2), \tag{8}$$

from which we can determine k_x for fixed k_y, k_z and the Fermi energy $E = E_F$. We are interested in the electron

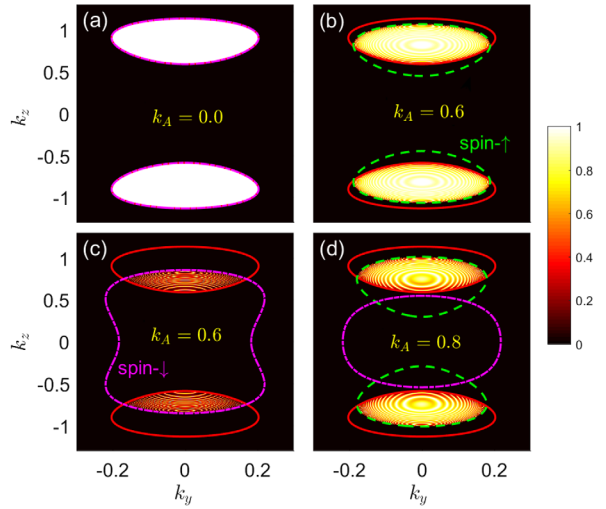

FIG. 3. Distribution of the spin-dependent transmission probabilities $T_\uparrow(k_y, k_z)$ and $T_\downarrow(k_y, k_z)$ on the $k_y - k_z$ plane, (a) for $k_A = 0$ where $T_\uparrow(k_y, k_z)$ coincides with $T_\downarrow(k_y, k_z)$ completely, (b),(c) for $k_A = 0.6$, and (d) for $k_A = 0.8$ where $T_\downarrow(k_y, k_z) = 0$. The lines represent the projections of the Fermi surfaces, with red solid, green dashed, and pink dashed-dotted lines for the reservoirs and the spin-↑ and spin-↓ components in the middle WSM region, respectively. Here, $E_F = 0.05$ eV, $d = 400$ nm, and $\phi = \pi/2$, and the other parameters are the same as in Fig. 2(a).

transport near the gap-closing points, so the unimportant terms $\epsilon_0(\mathbf{k})$ and $M_2(k_x^2 + k_y^2)$ can be neglected. It is easy to find the wave functions in different regions. By matching the wave functions at the interfaces $\psi_s(x{=}0^-){=}\psi_s(x{=}0^+)$ and $\psi_s(x = d^-) = \psi_s(x = d^+)$, we can obtain the transmission coefficient as

$$t_s = \frac{2\mathcal{F}_1\mathcal{F}_2 e^{-i[k_1+s(v_1/v_s)k_z\cos\phi]d}}{2\mathcal{F}_1\mathcal{F}_2\cos(k_2 d) - i(\mathcal{F}_1^2 + \mathcal{F}_2^2 + \Delta_y^2)\sin(k_2 d)}, \quad (9)$$

where k_1 represents the positive root of Eq. (8) and k_2 can be obtained from the eigenequation for the CPL-driven region. In Eq. (9), $\mathcal{F}_1 = v_0 k_1[E - \tilde{M}_s(\mathbf{k})]$, $\mathcal{F}_2 = v_s k_2 [E - M(\mathbf{k})]$, and

$$\Delta_y = v_0 k_y[E - \tilde{M}_s(\mathbf{k})] - v_s\tilde{k}_{y,s}[E - M(\mathbf{k})]. \quad (10)$$

The spin-dependent transmission probability can be obtained by $T_s(k_y, k_z) = |t_s|^2$. For $d \gg 1$, the transmission probability is finite only when $k_{1,2} \in$ real; i.e., k_y and k_z are within the overlapping region of the projected Fermi surfaces of the reservoirs and the CPL-driven WSM.

The distributions of the spin-dependent transmission probabilities $T_\uparrow(k_y, k_z)$ and $T_\downarrow(k_y, k_z)$ on the $k_y - k_z$ plane are plotted in Fig. 3. In the absence of CPL, $T_\uparrow(k_y, k_z) = T_\downarrow(k_y, k_z) = 1$ for all of the incident electron states, as shown in Fig. 3(a), because of the perfect matching of the

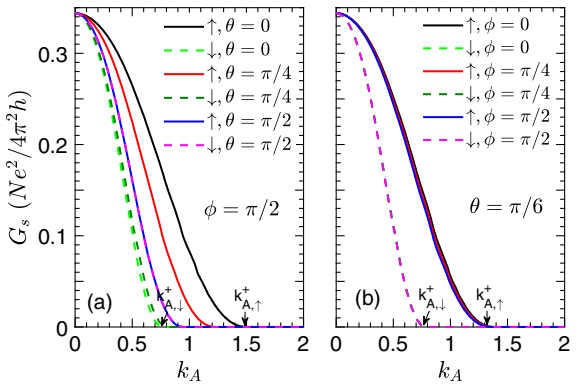

FIG. 4. Spin-dependent conductances $G_\uparrow$ and $G_\downarrow$ as a function of the CPL intensity k_A for (a) different θ with $\phi = \pi/2$ and for (b) different ϕ with $\theta = \pi/6$. Other parameters are the same as in Fig. 3.

Fermi surfaces between different regions. With the introduction of CPL, the Weyl nodes are split and move in the k_z axis, which leads to a mismatch of wave vectors between the middle region and the reservoirs [33,34]. Because of the broken TR symmetry, two spin species exhibit different splitting distances along k_z and thus different shapes of Fermi surfaces in Figs. 3(b) and 3(c). Consequently, the spin-↑ Fermi surface in the middle WSM region has a larger overlap with that in the DSM reservoirs (denoted by the red solid lines), whereas the spin-↓ Fermi surface has a smaller overlap. Naturally, there emerge interesting spin-dependent electron transport processes. With a further increase in irradiation intensity k_A, the spin-↓ Fermi surfaces in the middle region would disconnect from those of the reservoirs and thus make no contribution to the electron transport, as shown in Fig. 3(d). In this situation, there will emerge a fully spin-polarized current, implying that the irradiated region has entered WHM phase (1,0).

Fully spin-polarized conductance.—The spin-dependent conductance can be calculated using the Landauer formula,

$$G_s = \frac{e^2}{h}\sum_{k_y,k_z} T_s(k_y, k_z), \quad (11)$$

where the summation runs over all the incident modes at the Fermi surface, i.e., the $k_y - k_z$ surface BZ. In Fig. 4(a), we plot the spin-dependent conductance $G_\uparrow$ and $G_\downarrow$ as a function of the CPL intensity k_A for different polar angles θ. As k_A increases, the spin-dependent conductances $G_\uparrow$ and $G_\downarrow$ will decrease due to suppression of the transmission probability, and after certain thresholds, they vanish completely. Although both conductances reduce with k_A, $G_\downarrow$ decays with a faster rate than $G_\uparrow$ such that the threshold $k^+_{A,\downarrow}$ for a spin-↓ current is lower than the $k^+_{A,\uparrow}$ for a spin-↑ current. For $k_A \in (k^+_{A,\downarrow}, k^+_{A,\uparrow})$, the electric current is spin-↑ fully polarized, exhibiting a perfect spin filter effect. The spin filter region $(k^+_{A,\downarrow}, k^+_{A,\uparrow})$ is quite sensitive to the

incident direction θ of the CPL. As the polar angle deviates from $\theta = 0$, the spin filter region ($k^+_{A,\downarrow}$, $k^+_{A,\uparrow}$), as shown in Fig. 4(a), will be reduced. For a specific value $\theta = \pi/2$, there is no spin-polarized conductance because the WHM phase does not exist in this situation, as seen in Fig. 2(b). In contrast, the spin filter region, as shown in Fig. 4(b), is almost independent of the azimuthal angle ϕ of the CPL since the thresholds given by Eq. (7) are irrelevant with ϕ.

Conclusion and remarks.—We have theoretically studied the Floquet phase transition of $\mathbb{Z}_2$ topological DSMs subjected to a beam of CPL. Owing to the interplay of the chiral and $\mathbb{Z}_2$ charges, the Weyl nodes are not only chirality dependent but also spin dependent, which constrains the behavior in the creation and annihilation of a pair of Weyl nodes. During the evolution of Weyl nodes with CPL intensity, we have found an entirely new WHM phase: One spin band is in the WSM phase while the other spin band is in the insulator phase, which simultaneously possesses the characteristics of both WSMs and half-metals. This novel phase has not been reported before. We have also checked to see that an applied magnetic field or magnetic perturbation or linearly polarized light cannot achieve this WHM phase because it cannot realize the creation and annihilation of the Weyl node pair at the same time [29].

We have further studied the spin-dependent transport and have found a spin filter effect as a fingerprint of the existence of the WHM phase. Indeed, the spin filter transistor is an important device in spintronics, with numerous works focusing on its implementation using topological edge or surface states [35–39]. However, these have several typical shortcomings: (1) they experience disturbance from the unpolarized bulk band, (2) they easily suffer from magnetic disorder, and (3) they appear only at several specific energy positions, which is difficult to manipulate experimentally. Recently, Tsai *et al.* [40] proposed a silicene-based spin filter device to reduce the above shortcomings by taking advantage of the bulk carriers. Here, we have proposed the spin filter effect based on the WHM bulk band, in contrast to previous works.

In realistic experiments, one can realize our proposed model by using a beam of Gaussian profile light or replacing Weyl-semimetal reservoirs with normal-metal electrodes, as discussed in the Supplemental Material [29]. The threshold of the incident radiation intensity for the system entering the WHM phase has been determined with Eq. (7). For Na_3Bi [9], with $k_A = eA_0/\hbar$ and $A_0 = E_0/\omega$, we estimate the threshold of the irradiated electric field to be $E_0 \simeq 7.2 \times 10^8$ V/m for $\hbar\omega = 1$ eV. For Cd_3As_2 [41], the threshold can be reduced by an order of magnitude $E_0 \simeq 5 \times 10^7$ V/m for $\hbar\omega = 0.5$ eV. These radiation intensities are within current experimental accessibility [42,43].

This work was supported by the National Natural Science Foundation of China under Grants No. 11874016 and No. 11904107, by the Key Program for Guangdong NSF of China under Grant No. 2017B030311003, GDUPS (2017), by the State Key Program for Basic Research of China under Grants No. 2015CB921202 (L. S.) and No. 2017YFA0303203 (D. Y. X.), and by the Innovation Project of the Graduate School of South China Normal University.

X.-S. L. and C. W. contributed equally to this work.

*dengmingxun@scnu.edu.cn
†wangruiqiang@m.scnu.edu.cn
‡dyxing@nju.edu.cn

[1] N. P. Armitage, E. J. Mele, and A. Vishwanath, Rev. Mod. Phys. **90**, 015001 (2018).
[2] Z. K. Liu, B. Zhou, Y. Zhang, Z. J. Wang, H. M. Weng, D. Prabhakaran, S.-K. Mo, Z. X. Shen, Z. Fang, X. Dai, Z. Hussain, and Y. L. Chen, Science **343**, 864 (2014).
[3] B.-J. Yang and N. Nagaosa, Nat. Commun. **5**, 4898 (2014).
[4] E. V. Gorbar, V. A. Miransky, I. A. Shovkovy, and P. O. Sukhachov, Phys. Rev. B **91**, 121101(R) (2015).
[5] S. Raza, A. Sirota, and J. C. Y. Teo, Phys. Rev. X **9**, 011039 (2019).
[6] S. E. Han, G. Y. Cho, and E.-G. Moon, Phys. Rev. B **98**, 085149 (2018).
[7] M.-X. Deng, W. Luo, R.-Q. Wang, L. Sheng, and D. Y. Xing, Phys. Rev. B **96**, 155141 (2017).
[8] M. Neupane, S.-Y. Xu, R. Sankar, N. Alidoust, G. Bian, C. Liu, I. Belopolski, T.-R. Chang, H.-T. Jeng, H. Lin, A. Bansil, F. Chou, and M. Z. Hasan, Nat. Commun. **5**, 3786 (2014).
[9] Z. Wang, Y. Sun, X.-Q. Chen, C. Franchini, G. Xu, H. Weng, X. Dai, and Z. Fang, Phys. Rev. B **85**, 195320 (2012).
[10] Z. Wang, H. Weng, Q. Wu, X. Dai, and Z. Fang, Phys. Rev. B **88**, 125427 (2013).
[11] X. Wan, A. M. Turner, A. Vishwanath, and S. Y. Savrasov, Phys. Rev. B **83**, 205101 (2011).
[12] A. A. Burkov and Y. B. Kim, Phys. Rev. Lett. **117**, 136602 (2016).
[13] J. Xiong, S. K. Kushwaha, T. Liang, J. W. Krizan, M. Hirschberger, W. Wang, R. J. Cava, and N. P. Ong, Science **350**, 413 (2015).
[14] C.-Z. Li, L.-X. Wang, H. Liu, J. Wang, Z.-M. Liao, and D.-P. Yu, Nat. Commun. **6**, 10137 (2015).
[15] C. Zhang, E. Zhang, W. Wang, Y. Liu, Z.-G. Chen, S. Lu, S. Liang, J. Cao, X. Yuan, L. Tang, Q. Li, C. Zhou, T. Gu, Y. Wu, J. Zou, and F. Xiu, Nat. Commun. **8**, 13741 (2017).
[16] X. Huang, L. Zhao, Y. Long, P. Wang, D. Chen, Z. Yang, H. Liang, M. Xue, H. Weng, Z. Fang, X. Dai, and G. Chen, Phys. Rev. X **5**, 031023 (2015).
[17] M.-X. Deng, G. Y. Qi, R. Ma, R. Shen, R.-Q. Wang, L. Sheng, and D. Y. Xing, Phys. Rev. Lett. **122**, 036601 (2019).
[18] S. Liang, J. Lin, S. Kushwaha, J. Xing, N. Ni, R. J. Cava, and N. P. Ong, Phys. Rev. X **8**, 031002 (2018).
[19] M. Rogatko and K. Wysokinski, J. High Energy Phys. 09 (2018) 136.
[20] M. S. Rudner, N. H. Lindner, E. Berg, and M. Levin, Phys. Rev. X **3**, 031005 (2013).

[21] P. Titum, N. H. Lindner, M. C. Rechtsman, and G. Refael, Phys. Rev. Lett. **114**, 056801 (2015).
[22] A. Farrell and T. Pereg-Barnea, Phys. Rev. Lett. **115**, 106403 (2015).
[23] C.-K. Chan, P. A. Lee, K. S. Burch, J. H. Han, and Y. Ran, Phys. Rev. Lett. **116**, 026805 (2016).
[24] Z. Yan and Z. Wang, Phys. Rev. Lett. **117**, 087402 (2016).
[25] M.-X. Deng, W. Y. Deng, D. X. Shao, R.-Q. Wang, R. Shen, L. Sheng, and D. Y. Xing, Phys. Rev. B **95**, 115102 (2017).
[26] P.-H. Fu, H.-J. Duan, R.-Q. Wang, and H. Chen, Phys. Lett. A **381**, 3499 (2017).
[27] G. Chang, S.-Y. Xu, H. Zheng, B. Singh, C.-H. Hsu, G. Bian, N. Alidoust, I. Belopolski, D. S. Sanchez, S. Zhang, H. Lin, and M. Z. Hasan, Sci. Rep. **6**, 38839 (2016).
[28] C. Chen, Z.-M. Yu, S. Li, Z. Chen, X.-L. Sheng, and S. A. Yang, Phys. Rev. B **99**, 075131 (2019).
[29] See Supplemental Material at http://link.aps.org/supplemental/10.1103/PhysRevLett.123.206601 for a detailed derivation of Eq. (3) and a discussion of the dependence of the transmission probability and conductances on d, the role of an applied magnetic field or magnetic perturbation or a linearly polarized light, and two projects to observe the spin filter effect in an experiment.
[30] C. W. Groth, M. Wimmer, A. R. Akhmerov, and X. Waintal, New J. Phys. **16**, 063065 (2014).
[31] M. A. Sentef, M. Claassen, A. F. Kemper, B. Moritz, T. Oka, J. K. Freericks, and T. P. Devereaux, Nat. Commun. **6**, 7047 (2015).
[32] E. J. Sie, *Coherent Light-Matter Interactions in Monolayer Transition-Metal Dichalcogenides*, Springer Theses (Springer, Berlin, 2018).
[33] N. Stander, B. Huard, and D. Goldhaber-Gordon, Phys. Rev. Lett. **102**, 026807 (2009).
[34] A. F. Young and P. Kim, Nat. Phys. **5**, 222 (2009).
[35] A. Rycerz, J. Tworzydło, and C. W. J. Beenakker, Nat. Phys. **3**, 172 (2007).
[36] C. Brüne, A. Roth, H. Buhmann, E. M. Hankiewicz, L. W. Molenkamp, J. Maciejko, X.-L. Qi, and S.-C. Zhang, Nat. Phys. **8**, 485 (2012).
[37] R.-Q. Wang, L. Sheng, R. Shen, B. Wang, and D. Y. Xing, Phys. Rev. Lett. **105**, 057202 (2010).
[38] S. Rachel and M. Ezawa, Phys. Rev. B **89**, 195303 (2014).
[39] S. Zamani and R. Farghadan, Phys. Rev. Applied **10**, 034059 (2018).
[40] W.-F. Tsai, C.-Y. Huang, T.-R. Chang, H. Lin, H.-T. Jeng, and A. Bansil, Nat. Commun. **4**, 1500 (2013).
[41] A. Chen, D. I. Pikulin, and M. Franz, Phys. Rev. B **95**, 174505 (2017).
[42] Y. H. Wang, H. Steinberg, P. Jarillo-Herrero, and N. Gedik, Science **342**, 453 (2013).
[43] F. Mahmood, C.-K. Chan, Z. Alpichshev, D. Gardner, Y. Lee, P. A. Lee, and N. Gedik, Nat. Phys. **12**, 306 (2016).